PROGRESS IN NATURAL SCIENCE Vol. 17, No. 1, January 2007

Design and implementation of an optical simulation environment for bioluminescent tomography studies*

LI Hui[1,2], TIAN Jie[2]**, LUO Jie[2], LÜ Yujie[2], CONG Wenxiang[3] and WANG Ge[3]

(1. Department of Education Technology, Capital Normal University, Beijing 100037, China; 2. Key Laboratory of Complex Systems and Intelligence Science, Institute of Automation, Chinese Academy of Sciences, Beijing 100080, China; 3. Bioluminescent Tomography Laboratory, Department of Radiology & Department of Biomedical Engineering, University of Iowa, Iowa City, Iowa 52242, USA)

Accepted on May 24, 2006

Abstract As a challenging task for bioluminescent tomography simulation, a virtual optical environment is needed to solve the forward problem accurately, that is, to achieve a high precision for bioluminescent signal synthesis on the external body surface of a small animal. The molecular optical simulation environment named MOSE is implemented using the C++ programming language and the OpenGL techniques, including a user-friendly interface with interactive tools facilitating users' operations. The accuracy of the virtual optical environment is verified by error analysis of mesh simplification and comparison between MOSE results and experimental data. This virtual optical environment is accurate, flexible and efficient to simulate the photon propagation in complicated tissues, which has a great potential to become a software platform for bioluminescent tomography studies and other molecular imaging applications.

Keywords: molecular imaging, bioluminescent tomography, photon propagation, Monte Carlo method.

With the development of biological and optical techniques, *in vivo* bioluminescent imaging attracts more attention for non-invasively monitoring the physiological and pathological processes of biological tissues in real-time[1—4]. As an important aspect of our bioluminescent tomography project, an optical simulation software platform named MOSE[5] was developed to simulate bioluminescent phenomena in small living animals (e.g. the mouse), specifically to predict bioluminescent signals on the body surface of the animal. It is challenging to build a virtual optical simulation environment to describe the interactions between the complicated biological tissues and bioluminescent photon packets. A number of optical simulation platforms (e.g. MCNP, EGS4, MCML, and TracePro) are available, but at a certain point such interactive mechanisms are lacking[6—8]. Here, we report the major enhancement towards our earlier MOSE[5] platform to improve the flexibility, precision and efficiency of bioluminescent tomography simulation, leading to the virtual optical environment with a relatively complete array of image processing algorithms and graphic editing tools.

Compared with our first version of MOSE, a key improvement lies in that the input is not only the simulated phantom data but also the real micro-CT images. After data preprocessing and 3D image processing (e.g. image segmentation, image reconstruction, surface rendering), a biological model is generated in terms of a series of triangular meshes. Moreover, several interactive graphic editing tools are used to flexibly generate and manipulate the bioluminescent sources. After millions of photon propagation steps in the virtual optical environment simulated by the Monte Carlo method, bioluminescent signals viewed by CCD detectors and other physical quantities can be conveniently obtained. As a whole, the simulation of the photon propagation is made significantly more realistic and flexible by the second version of the MOSE than that allowed by the first version.

In this article, we first describe the second version of the MOSE, then report an error analysis with respect to mesh simplification and comparison with experimental data. Finally, we conclude the paper with the software download information.

1 Theory and methods

1.1 Small animal geometrical modeling

To build a small animal geometrical model, a se-

---

* Supported by National Natural Science Fundation for Distinguished Young Scholars of China (Grant No. 60225008), National Natural Science Foundation of China (Grant Nos. 30500131, 90209008, 30370418, 60302016), and the National Institutes of Health, USA (Grant No. EB001685)

** To whom correspondence should be addressed. E-mail: tian@doctor.com, lihui@fingerpass.net.cn ries of CT slices or image volume are taken as the input of the software MOSE. The prerequisite parameters of the input include image width/height of each slice, the total number of slices, the inter-slice distance, and the optical properties of biological tissues. With 3D imaging processing algorithms (e.g. surface rendering, mesh simplification), any irregular biological tissue can be described by a series of triangular meshes. The virtual biological environment is completed after the combination of all biological tissues.

1.1.1 Surface rendering Any organ can be segmented from the slices by an appropriate segmentation algorithm according to its gray level range. Then, triangular meshes will be obtained by a marching cubes algorithm to describe its geometrical shape, which is referred to as surface rendering. With the segmentation and surface rendering algorithms, all the tissue surface whose grey levels are between the gray level range (i.e. $TG_{\min}$ and $TG_{\max}$) can be reconstructed. Fig. 1 presents the bone surface, the heart surface, and the combined surfaces of several organs obtained with surface rendering. When each organ is expressed by triangular meshes, the whole virtual biological environment (Fig. 1 (c)) is formed by combining all the meshes. The 3D image processing algorithms (e.g. segmentation, re-slice, surface rendering) are adapted from the Medical Imaging ToolKit (MITK)[9] developed by MIPG, Institute of Automation, Chinese Academy of Sciences (http://www.mitk.net).

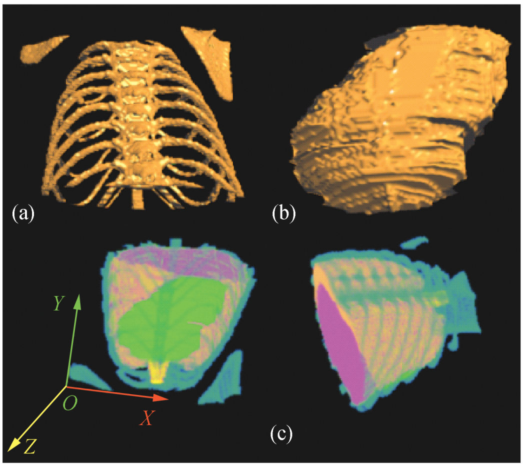

Fig. 1. Virtual biological environment. (a) Skeletal structure; (b) heart; (c) combined renderings of the mouse thorax.

1.1.2 Mesh simplification In general, there are millions of triangular meshes describing each organ of the mouse thorax after surface rendering. It is well known that the more triangular meshes are used, the longer time is needed for the photon propagation simulations. It is critical to simplify the triangular meshes for practical application. In the new version of the MOSE, a fast mesh simplification algorithm combining the half-edge data structure and modified Quadric Error Metrics (QEM), is used to simplify the original triangular meshes.

The original QEM is first advanced by Garland and Heckbert in 1997[10] and it has been widely applied in computer graphics field. However, its primary deficiency is that the triangular meshes of the smooth renconstructed surface are apt to be simplified. The modified QEM with an updated distance function is used here to ensure the simplicity.

The cost function of the QEM is based on the Euclidean distance, and it decides the collapsing sequences of all the half-edges. The distance $D_M(\boldsymbol{v})$ between any vertex P whose vector is $\boldsymbol{v}=[x \quad y \quad z]^{\mathrm{T}}$ and any triangular mesh plane M whose equation is $\boldsymbol{n}^{\mathrm{T}}\boldsymbol{u}+d=0$ satisfies

$$\begin{aligned} D_M^2(\boldsymbol{v}) &= (\boldsymbol{n}^{\mathrm{T}}\boldsymbol{v}+d)^2 \\ &= \boldsymbol{v}^{\mathrm{T}}(\boldsymbol{n}\boldsymbol{n}^{\mathrm{T}})\boldsymbol{v} + 2(d\boldsymbol{n})^{\mathrm{T}}\boldsymbol{v} + d^2 = \boldsymbol{v}'^{\mathrm{T}}\boldsymbol{Q}_M\boldsymbol{v}', \end{aligned} \tag{1}$$

where $\boldsymbol{n}$ is the unit normal of the plane, 4×4 matrix $\boldsymbol{Q}_M=\begin{bmatrix}\boldsymbol{A} & \boldsymbol{b}\\ \boldsymbol{b}^{\mathrm{T}} & c\end{bmatrix}$ is the error matrix, $\boldsymbol{A}=\boldsymbol{n}\boldsymbol{n}^{\mathrm{T}}$ is a 3×3 matrix, $\boldsymbol{b}=d\boldsymbol{n}$ is a 1D vector, $c=d^2$ is a constant, and $\boldsymbol{v}'=[x \quad y \quad z \quad 1]^{\mathrm{T}}$.

In addition to all the adjacent triangular elements associated with the vertex P, considering the characteristics of medical images, the normal vector of the tangential plane of P is a prerequisite parameter to calculate the distance function $D(v)$ by

$$D^2(\boldsymbol{v}) = \sum_i w_i D_i^2(\boldsymbol{v}) + w_T D_T^2(\boldsymbol{v}) = Q(\boldsymbol{v}), \tag{2}$$

where $D_i(\boldsymbol{v})$ denotes the Euclidean distance between P and the ith triangular element involving P; $D_T(\boldsymbol{v})$ denotes the Euclidean distance between P and its tangential plane T; $w_i = S_i / \sum_i S_i$ represents the weight of the ith mesh whose area is S_i; weight w_T is usually chosen according to the number of the triangular meshes involving vertex P.

Therefore, the cost of collapsing the half-edge P_1P_2 is presented by the cost function $E_Q(\boldsymbol{v})=$

$D^2(\boldsymbol{v}_1)+D^2(\boldsymbol{v}_2)=Q(\boldsymbol{v}_1,\boldsymbol{v}_2)$. Then, the optimal point P' is calculated to minimize the cost function, which is the new point after collapsing the half-edge P_1P_2. If matrix $\boldsymbol{A}$ is a nonsingular one, the coordinates of new vertex p' can be expressed as $\boldsymbol{v}'=-\boldsymbol{A}^{-1}\boldsymbol{b}$ satisfying a group of partial differential equations $\partial Q/\partial x=\partial Q/\partial y=\partial Q/\partial z=0$. Then, the cost of collapsing P_1P_2 is calculated by $Q(\boldsymbol{v})=-\boldsymbol{b}^{\mathrm{T}}\boldsymbol{A}^{-1}\boldsymbol{b}+c$. If matrix $\boldsymbol{A}$ is singular, a point P' on the half-edge P_1P_2, whose coordinates minimize $E_Q(\boldsymbol{v}')$, can be chosen as the new vertex. If $(v_1-v_2)^{\mathrm{T}}\boldsymbol{A}(v_1-v_2)\neq 0$, the optimal vertex coordinates $\boldsymbol{v}'$ is calculated by the following equations

$$\boldsymbol{v}'=a(\boldsymbol{v}_1-\boldsymbol{v}_2)+\boldsymbol{v}_2,$$

$$a=-\frac{(\boldsymbol{v}_1-\boldsymbol{v}_2)^{\mathrm{T}}\boldsymbol{A}\boldsymbol{v}_2+\boldsymbol{v}_2^{\mathrm{T}}\boldsymbol{A}(\boldsymbol{v}_1-\boldsymbol{v}_2)+2\boldsymbol{b}(\boldsymbol{v}_1-\boldsymbol{v}_2)}{2(\boldsymbol{v}_1-\boldsymbol{v}_2)^{\mathrm{T}}\boldsymbol{A}(\boldsymbol{v}_1-\boldsymbol{v}_2)}, \tag{3}$$

where $0\leqslant a\leqslant 1$. If the optimal vertex cannot be computed in this way, the new vertex is chosen from P_1, P_2 and their average, which minimizes $E_Q(\boldsymbol{v}')$.

The information on all the half-edges can be stored into a heap according to their collapse costs. When the mesh simplification is performing, the half-edge with the minimum cost on the heap is first chosen. This method promises the minimum simplification error and accelerates the process of mesh simplification. The experiments confirm that the initialization speed is 2 times faster than that with the original QEM, and the simplification speed is 2—4 times faster than that with the original QEM.

1.1.3 Characteristic function

When a photon is generated or moves to a new position, the characteristic function identifies whether or not it is in a given organ. This function is repeatedly performed through the whole process of the photon propagation. The accuracy and efficiency of the function significantly influence the performance of the MOSE. Various strategies are applied to different situations in order to achieve fast speed and high accuracy.

As an important building block, polygons formed by lines or arcs are taken to describe the 2D biological simulation environment. A strategy based on the Jordan Curve Theorem is introduced to judge the relationship between a photon and organs. Essentially, it indicates that a point is inside a polygon if, for any ray from this point, there is an odd number of crossings between the ray with the polygonal edges. This theorem suggests the so-called crossings test[11] (Fig. 2). According to that rule, when the test ray intersects one or more vertices of the polygon, the crossing point at the vertex will be counted twice. Then, the test may fail in this situation. This problem can be resolved by a modified strategy as follows. Whenever the test ray intersects a vertex, it is always classified as being infinitesimally above the ray, and so no vertices are intersected.

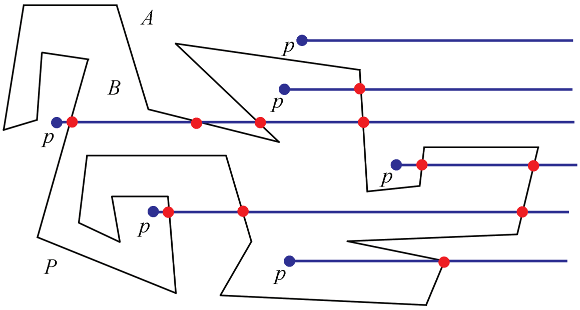

Fig. 2. Crossing test. Polygon P divides the points of the plane into sets A and B. From each test point p, shoot a ray along $+X$ axis, and count the intersection points.

In the MOSE, 3D biological tissues and bioluminescent sources are described by a series of triangular meshes. Hence, the whole 3D biological simulation environment is made up of a number of polyhedrons. Then, the 2D characteristic function can be extended to the 3D case based on the same theory. When a test ray from point p intersects an edge or a vertex, we perturb p slightly, and apply the crossing test strategy to judge the relationship between p and meshed models.

1.2 Graphic editing tools

At various stages of pathologic manifestations, the actual bioluminescent sources in biological tissues are usually irregular. Therefore, several graphic editing tools are developed to define the bioluminescent sources and to modify the local contours of original sources.

1.2.1 Superquadrics

The superquadric models were introduced into computer graphics fields in 1981[12,13]. Among four types of superquadric models (i. e. superellipsoid, supertoroid, and superhyperboloid with one or two sheets), only the superellipsoid defines a closed surface without holes, which is always consistent with the real biomedical structures. Hence, the superellipsoid is commonly referred to as the superquadric and is used as a building block in our simulation platform. It is easy to judge whether a point $p(x,y,z)$ is in a given superellipsoid or not according to the characteristic function $F(x,y,z) = (|x/r_x|^{2/\varepsilon_2} + |y/r_y|^{2/\varepsilon_2})^{\varepsilon_2/\varepsilon_1} + |z/r_z|^{2/\varepsilon_1}$, where radius parameters r_x, r_y, r_z denote the scaling factors on x, y and z axes, squareness parameters ε_1, ε_2 are the shape parameters related to the squareness/roundness/pinchedness in the longitudinal and horizontal directions, respectively. More discussions are presented in Refs. [14,15].

1.2.2 2D graphic editing tools In the 2D simulation environment, any irregular objects can be described by 2D interactive graphic editing tools and can be iteratively modified. 2D shapes of the bioluminescent sources are usually determined by smoothly connecting the adjoining vertexes on the contour with polynomial curves or arcs. With the interactive graphic editing tools, the original contour of sources can be changed by adding, deleting, and moving vertexes. Generally, if one part of the local contour is smooth, fewer vertexes are sufficient to depict its features; if it is rough (e.g. sharp protuberances), more vertexes are needed to describe the details.

1.2.3 3D graphic editing tools Initial shapes of 3D bioluminescent sources are usually chosen as spheres or cylinders whose parameters are determined according to the prior knowledge. As an interactive editing tool in the MOSE, the Bezier cubic spline is applied to modify the local 3D shapes. First, the volume of interest (VOI) of the bioluminescent source is selected, which defines the local surface S_L to be modified. Then, the selected local surface can be interactively altered with the movement of a control point p_c along any direction. The default position of the original control point p_c is determined by the shape of the local surface S_L. When the location of the point p_c is changed, the selected local surface inside the VOI is updated to a new series of Bezier cubic splines. The mechanism for 2D Bezier cubic spline curve and 3D surface modification is introduced in detail in Refs. [16,17] and schematically described in Fig. 3.

1.3 Photon propagation

After the virtual optical simulation environment is built, photon packets generated by bioluminescent sources will propagate therein. Position-sample, angle-sample and energy-sample are the three requisite steps for the photon packet generation. Given the intensity distribution of sources, the Monte Carlo method is used to sample these parameters[18,19]. It is assumed that these sources are uniformly distributed in certain 3D areas without losing generality.

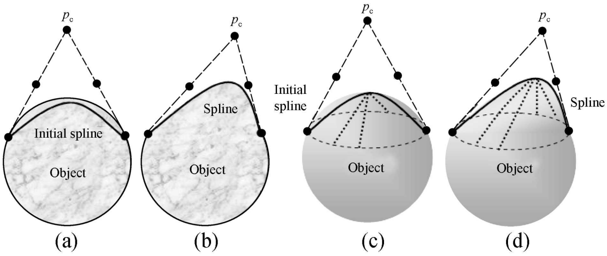

Fig. 3. Schematic diagram of the local surface modified by the control point p_c according to Bezier cubic splines. (a) 2D surface of the original object with the initial spline determined by the control point p_c; (b) the modified surface of the object with the dragged spline generated by the new control point; (c) 3D surface of the original object with a series of initial splines determined by the control point p_c; (d) the modified surface with a group of dragged splines generated by the new control point.

The photon propagation process includes several key steps, such as photon movement, absorption, scattering, termination, etc., which were described at the first version of the MOSE[5]. Photon generation and boundary behavior are emphasized as follows.

1.3.1 Photon generation Since position-, direction- and energy-sampling produce initial parameters of photon packets with the first two steps already described[5], energy-sampling is emphasized here. Because optical properties of any biological organ are wavelength/energy dependent, the spectrum of multi-spectral bioluminescent sources is split into N (e.g. $N=32$) consecutive bins in the Monte Carlo simulation. Photon packets generated in the same bin are assumed to have the same wavelength/energy. As all the energy levels are uniformly distributed, there are two ways to perform the simulation. One is to simulate the photon packets at each energy level, and the other is to obtain the energy level of each photon packet by using the energy sample. After the propagation processes of all the photon packets terminate, the transmitted and absorbed intensity distribution are recorded at various energy levels. According to the uniform distribution and the Monte Carlo method, the energy level can be sampled by $E = \mathrm{Int}(N\xi_E)$, where ξ_E is a pseudo-random number uniformly distributed over the interval from zero to one, N is the total number of consecutive bins, and $\mathrm{Int}(x)$ returns the largest integer that is less than or equal to x.

1.3.2 Boundary effect During the transportation of a photon packet, it may hit the boundary of the current tissue type, where the boundary may either be an interface between the tissue and the ambient medium or between the current and another tissue type. The photon packet can either be internally reflected back into the current tissue or transmit across the boundary depending on the incidence angle and so on. Given an incident directional vector $\boldsymbol{I}$ and a unit normal vector $\boldsymbol{N}$ at the boundary point, the internally reflected directional vector $\boldsymbol{R}$ or transmitted vector $\boldsymbol{T}$ can be calculated according to the vector schematics shown in Fig. 4. Then, the direction of photon propagation (μ_x, μ_y, μ_z) can be calculated as described before[5].

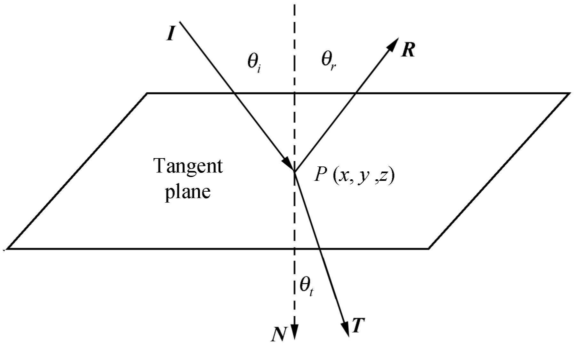

Fig. 4. Geometry of photon internal reflection and transmission at a tissue boundary. Unit vectors $\boldsymbol{I}$, $\boldsymbol{R}$ and $\boldsymbol{T}$ represent the direction vectors of incident, internally reflected and transmitted photons, respectively. Vector $\boldsymbol{N}$ represents the outside normal direction of the tangent plane at point $P(x, y, z)$.

1.4 Software design

1.4.1 User-friendly interface The updated MOSE version provides more powerful functions and a more friendly interface handling input parameters, output files, displays, and so on. All the functions are implemented with the C++ programming language and OpenGL techniques. In particular, the programs are integrated into the same program framework for 2D/3D simulation with geometric building blocks. These modes can be switched by pressing buttons on the toolbar.

After preprocessing the input data obtained from micro-CT, each biological organ and the whole subject such as a mouse can be iteratively displayed. Then, bioluminescent sources inside biological tissues are added in the simulated environment. With the control panel of the interface and the graphic editing tools, an operator can modify shapes of the initial sources. Before the optical simulation, one of the display modes of the photon propagation is selected: tracing all the photon propagation paths; only tracing those photons that reach detectors; or only tracing the photons with selected indices. Then, the whole photon propagation process is observed in real-time. The transport paths of different photon packets are highlighted in different colors. While tracing photon packets, the operator may stop or restart the display of tracing by pressing a switch at any moment. Once the simulation is finished, output files can be retrieved, containing absorption and/or transmission data, running time, and so on. When a pseudo color scheme is chosen, the distribution maps of absorption and transmission can be graphically displayed. As dynamic data allocation is employed, the parameters of biological tissues, bioluminescent sources and CCD detectors can be varied any time provided that the total amount of memory needed does not exceed the maximum allowance.

1.4.2 Search strategy In general, the simulated biological environment is quite complicated, because there are several organs described by triangular meshes. As a result, it is time-consuming to find the right organ containing a given point. Two table search strategies are utilized to improve the computational efficiency.

After preprocessing the input data obtained from micro-CT, the bounding-box of each biological organ is calculated, which includes the minimum and maximum values of the organ along three Cartesian coordinates. According to bounding-boxes and indices of the organs, two tables $\boldsymbol{T}_1$ and $\boldsymbol{T}_2$ are generated, respectively. Table $\boldsymbol{T}_1$ is a 3D matrix with the same size of the voxel matrix, each of whose values is the index of the biological organ containing the corresponding voxel. Table $\boldsymbol{T}_2$ reduces the number of triangular meshes to be searched when calculating the intersection between a photon and the tissue boundary. The whole simulated biological environment are divided into a number of independent regions as needed. All the indices of the triangular meshes in each region are saved into Table $\boldsymbol{T}_2(i)$, $1 \leqslant i \leqslant M$. If a photon hits the tissue boundary in region j, only the indices recorded in $\boldsymbol{T}_2(j)$ will be used to calculate the intersection. Clearly, the search space for triangular meshes is remarkably reduced by applying $\boldsymbol{T}_1$ and $\boldsymbol{T}_2$.

2 Experimental results

2.1 Error analysis on mesh simplification

As the triangular meshes are simplified, the running speed of the MOSE is improved accordingly. To precisely perform the MOSE simulation, the mesh simplification error must be analyzed. The geometric similarity metrics (GSM) is used to describe the impact of the procedure.

The first GSM is defined as $E_{\max}(M_1, M_2) = \max(\max_{v \in M_1} d_v(M_2), \max_{v \in M_2} d_v(M_1))$, where $d_v(M) = \min_{w \in M} \| v - w \|$ denotes the distance between the vertex v and a tissue model M defined by a series of triangular meshes, $\| \cdot \|$ means the Euclidean distance between two vectors. This GSM is applied to obtain the maximum error between the original tissue model M_1 and the simplified tissue model M_2. If the metrics satisfy $E_{\max}(M_1, M_2) \leqslant \varepsilon$, all the new vertexes in M_2 generated by the mesh simplification are located in the ε scope of the vertexes of the original tissue model M_1, and *vice versa*.

The second GSM is defined as

$$E_{\text{mean}}(M_1, M_2) = \frac{1}{2}\left(\frac{1}{V_{M_1}} \sum_{v \in M_1} d_v(M_2) + \frac{1}{V_{M_2}} \sum_{v \in M_2} d_v(M_1)\right),$$

where V_M is the number of the vertexes of the tissue model M. This GSM presents the average error between the original and simplified models. Hence, the value of the first GSM is generally larger than the second GSM. Nevertheless, the second GSM describes the mesh simplification error more efficiently. Furthermore, a relative error measure of the mesh simplification can be defined as $E_r = E_{\text{mean}}(M_1, M_2)/D_{\min}$, where $D_{\min}$ is the minimum dimension of the bounding-box for a given biological organ. The smaller the number of triangular elements is, the larger E_r is. If $E_r \leqslant 1\%$, the mesh simplification is practically acceptable. In our studies, E_r is usually chosen as 1%.

In the following experiment, the input to the MOSE is a 145×122×86 volume from 86 CT slices. The voxel dimensions are 0.156, 0.156, and 0.1428 mm, respectively. With the above-described algorithms, the geometric model of the mouse thorax is obtained (Fig. 1). With respect to each of the biological organs (e.g. mouse muscle, lung, heart, bone), the average errors between the original and simplified tissue models are presented in Fig. 5. Table 1 presents the relative error of the mesh simplification for each biological organ.

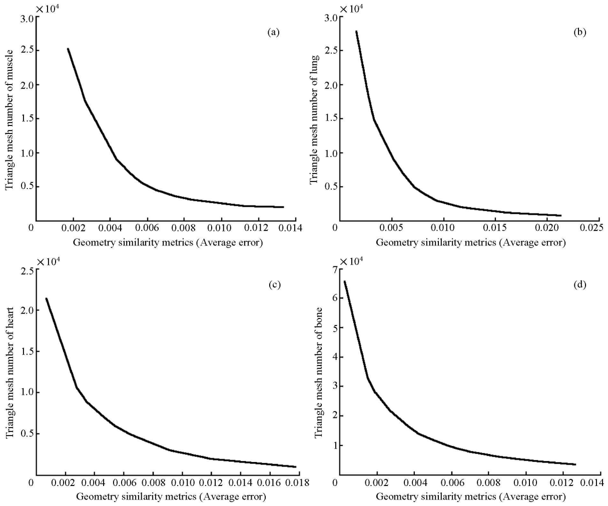

Fig. 5. Error analysis of mesh simplification. The geometric similarity metrics represents the average error between the original tissue model and the simplified one. Relationships between the average error and the triangular number in mesh simplification for (a) muscle, (b) lungs, (c) heart, and (d) bone.

Table 1. Mesh number and relative error after mesh simplification

Tissue	$D_{\min}$(mm)	Original mesh number	Target mesh number	Relative error
Muscle	12.4236	147788	2641	0.009678
Lung	10.7314	80784	2978	0.009301
Heart	7.8064	32200	1990	0.010011
Bone	12.2332	99184	5981	0.010042

2.2 Comparison with experimental data

To verify the MOSE software, two experiments are designed to compare numerical data with the real counterparts. The parameters of bioluminescent sources, phantom components and CCD detectors are shown in Tables 2, 3 and 4, respectively. In the experiments, ten simulations are performed with the given bioluminescent sources. Each simulation uses 100000 photon packets.

Statistically, the error inherent in the Monte Carlo simulation can be estimated. With a large sample number N, the relative error of the MOSE can be calculated by $R = \sqrt{\frac{\overline{x^2} - \bar{x}^2}{N}} \Big/ \bar{x}$, where $\bar{x} = E(x) = \int x p(x) \mathrm{d}x$ is the expected value of the random vari-

Table 2. Bioluminescent source parameters used in comparison between the MOSE and three phantom studies

Experiment No.	Sources No.	Shape	Center (mm)	Radius (mm)	Height (mm)	Photon number	Total power (nW)
1	1	cylinder	(−10, 0, 0)	0.50	1.00	1.0e+6	
2	2	cylinder	Source1: (−9.0, 1.5, 0) Source2: (−9.0, −1.5, 0)	0.28	1.90	1.0e+6	Source1: 85 Source1: 79

Table 3. Biological tissue parameters used in comparison between the MOSE and three phantom studies

Experiment No.	Center of outer cylinder	Radius of base (mm)	Height (mm)	Organ model	Absorption coefficient (mm^{-1})	Scattering coefficient (mm^{-1})	Refractive index	Anisotropy coefficient
1	(0, 0, 0)	15.0	30	Muscle	0.1000	3.00	1.37	0.800
2	(0, 0, 0)	15.0	30	Muscle	0.0068	10.31	1.37	0.900
				Lung	0.0233	20.00	1.00	0.906
				Heart	0.0104	10.96	1.37	0.910
				Bone	0.0001	3.00	1.37	0.980

Table 4. CCD detector parameters used in comparison between the MOSE and three phantom studies

Experiment No.	Shape	Center (mm)	Height (mm)	Width (mm)	Each pixel size (μm)
1	Rectangle	Design 1 (−15.5, 0, 0) Design 2 (0, 15.5, 0)	31.5	31.5	38
2	Rectangle	Design 1 (16.2, 0, 0) Design 2 (0, 16.2, 0) Design 3 (−16.2, 0, 0) Design 4 (0, −16.2, 0)	31.5	31.5	38

able x, $\overline{x^2}$ is calculated by the formula $\overline{x^2} = \int x^2 p(x)\mathrm{d}x$, and $p(x)$ is the probability density function of the random variable x.

In the first experiment, a cylindrical homogeneous tissue model with diameter of 30 mm and height of 30 mm is fabricated. With a volume source located in the tissue and two rectangle CCD detector planes parallel to the principal axis of the cylindrical tissue, we obtain both the experimental and numerical transmission profiles on CCD detectors as shown in Fig. 6. These figures indicate that the profiles of the MOSE are not as smooth as the experimental ones, since the photon number used in the Monte Carlo simulation is not sufficiently large. However, these two types of profiles are in excellent agreement. The more photons are traced, the more accurate match will be obtained in the corresponding profiles.

Based on the relative positions of the two sources and the detector plane, there are various combinations in the second experiment. Some representative data are provided as follows. Reconstructed from a series of CT slices (Fig. 7 (b)), a cylindrical 3D heterogeneous mouse chest phantom (Fig. 7 (a)) includes heart, lungs, bone, and muscle. All the optical parameters of the mouse chest phantom are based on *ex vivo* data as summarized in Table 3. The parameters of the two bioluminescent sources and the CCD detector plane are given in Tables 2 and 4, respectively. There are four configurations of the sources and detectors as shown in Fig. 7 (c). The numerical and experimental profiles are respectively indicated in Figs. 7 (d) and 7(e). These data confirm that all the corresponding results are very consistent.

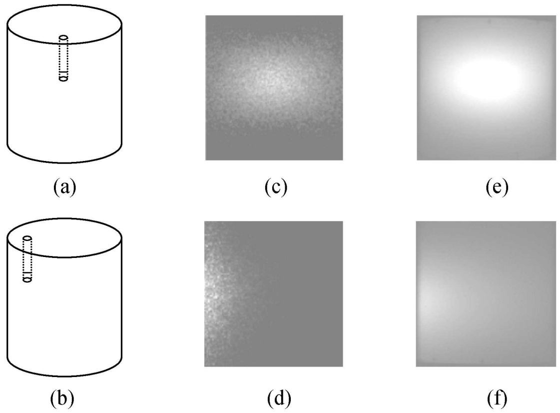
(a) (c) (e)
(b) (d) (f)

Fig. 6. First phantom experiment with one bioluminescent source and one cylindrical tissue ((a), (b)), the measurement data simulated using the MOSE ((c), (d)) and those really measured data ((e), (f)). The detector plane is located in the front of the cylindrical phantom. Parameters of cylindrical tissue, bioluminescent sources and CCD detectors are given in Tables 2, 3 and 4, respectively.

3 Conclusion

The MOSE is a PC-based 2D/3D simulator to predict bioluminescent signals detected by the CCD camera. Given a bioluminescent source inside the biological tissues and their optical parameters, the

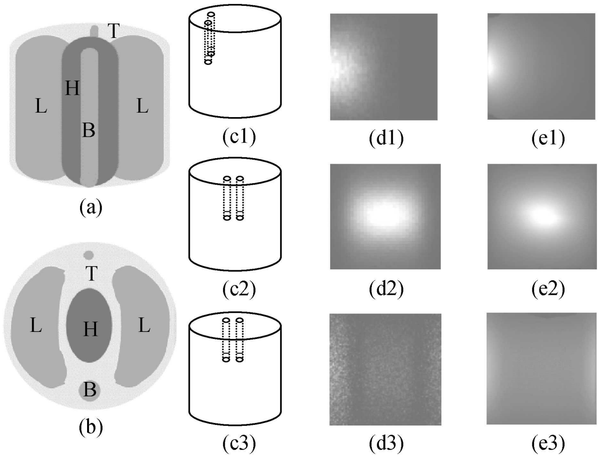

(a)　(b)　(c1)　(d1)　(e1)　(c2)　(d2)　(e2)　(c3)　(d3)　(e3)

Fig. 7.　Second phantom experiment with two bioluminescent sources and the mouse thorax phantom. （a） A heterogeneous mouse thorax phantom including bone （B），heart （H），lung （L） and tissue （T）；（b） a middle cross section of two hollow cylinders for hosting fluorescent sources in the left lung. With differently relative positions of the two sources and the detector plane （（c1），（c2），（c3）），the measurement data from MOSE （（d1），（d2），（d3）） and those really measured data （（e1），（e2），（e3）） can be obtained. The detector plane is in the front of the cylindrical tissue phantom. The parameters of the cylindrical tissue phantom，bioluminescent sources and CCD detectors are given in Tables 2，3 and 4，respectively.

MOSE mimics the propagation process of each photon packet using the Monte Carlo method. The key improvement of the second MOSE version （versus the first one） lies in that the input includes not only the simplified phantom data but also real raw CT or micro-CT data. The virtual biological environment can be built from the raw CT data in terms of a series of triangular elements，followed by preprocessing the input data. Interactive graphic editing tools are now available to define complicated bioluminescent sources iteratively. The error analysis on the mesh simplification has provided valuable information on bioluminescent imaging，and revealed the excellent performance of the MOSE.

The MOSE package and complete documents can be downloaded from the dedicated website http：//www.mosetm.net，or obtained from the corresponding authors.

References

1　Ntziachristos V.，Ripoll J.，Wang L. V. et al. Looking and listening to light：the evolution of whole-boday photonic imaging. Nature Biotechnology，2005，23：313—320.

2　Wang G.，Hoffman E. A.，McLennan G. et al. Development of the first bioluminescent CT scanner. Radiology，2003，229：566.

3　Wang G.，Li Y. and Jiang M. Uniqueness theorems in bioluminescence tomography. Medical Physics，2004，31：2289—2299.

4　Contag C. H. and Bachmann M. H. Advances in in vivo bioluminescence imaging of gene expression. Annual Review Biomedical Engineering，2002，4：235—260.

5　Li H.，Tian J.，Zhu F. P. et al. A mouse optical simulation environment （MOSE） to investigate bioluminescent phenomena in the living mouse with the Monte Carlo method. Academic Radiology，2004，11：1029—1038.

6　Wang L. H.，Jacques S. L. and Zheng L. Q. MCML—Monte Carlo modeling of light transport in multi-layered tissues. Computer Methods and Programs in Biomedicine，1995，47：131—146.

7　Briesmeister J. F. MCNP^{TM}—a general Monte Carlo N-Particle transport code，Version 4C. http：//mcnpx.lanl.gov ［2006-01-20］

8　Bielajew A. F.，Hirayama H.，Nelson W. R. et al. History，overview and recent improvements of EGS4. http：//www.slac.stanford.edu/egs/docs/pdf/nrcpirs0436.pdf ［2006-01-20］

9　Zhao M.，Tian J.，Zhu X. et al. Design and implementation of a C++ toolkit for integrated medical image processing and analyzing. In：Proceedings of the SPIE Medical Imaging. San Diego，USA，February 15—17，2004，39—47.

10　Garland M. and Heckbert P. S. Surface simplification using quadric error metric. In：Proceedings of SIGGRAPH ’97. Los Angeles，USA，August 3—8，1997，209—216.

11　Shimrat M. Algorithm 112：Position of point relative to polygon. Communications of the ACM，1962，5：434.

12　Barr A. H. Superquadrics and angel preserving transformations. IEEE Computer Graphics and Applications，1981，1：11—23.

13　Barr A. H. Global and local deformations of solid primitives. Computer Graphic，1984，18：21—30.

14　Sinnott J. and Howard T. SQUIDS：interactive deformation of superquadrics for model matching in virtual environment. In：Eurographics UK Conference. Swansea，UK，April 4—6，2000，73—80.

15　Zhu J. H.，Zhao S. Y.，Ye Y. B. et al. Computed tomography simulation with superquadrics. Medical Physics，2005，32：3136—3143.

16　Kang Y.，Engelke K. and Kalender W. A. Interactive 3D editing tools for image segmentation. Medical Image Analysis，2004，8：35—46.

17　Joy K. I. Bernstein polynomials. http：//graphics.cs.ucdavis.edu/education/CAGDNotes/Bernstein-Polynomials/Bernstein-Polynomials.html ［2006-01-20］

18　Wang L. H. and Jacques S. L. Monte Carlo modeling of light transport in multi-layered tissues in standard C. http：//omlc.ogi.edu/pubs/pdf/man_mcml.pdf ［2006-01-20］

19　Lux I. and Koblinger L. Monte Carlo Particle Transport Methods：Neutron and Photon Calculations. Florida：CRC Press，1991.